RSC Advances

ROYAL SOCIETY OF CHEMISTRY

www.rsc.org/advances

RSC Advances

RSCPublishing

ARTICLE

Table of Contents

Photothermal properties of GNSs and GNRs are compared both experimentally and theoretically, and results show that GNS exhibit higher molar heating rate than GNR.

Abstract Graphic

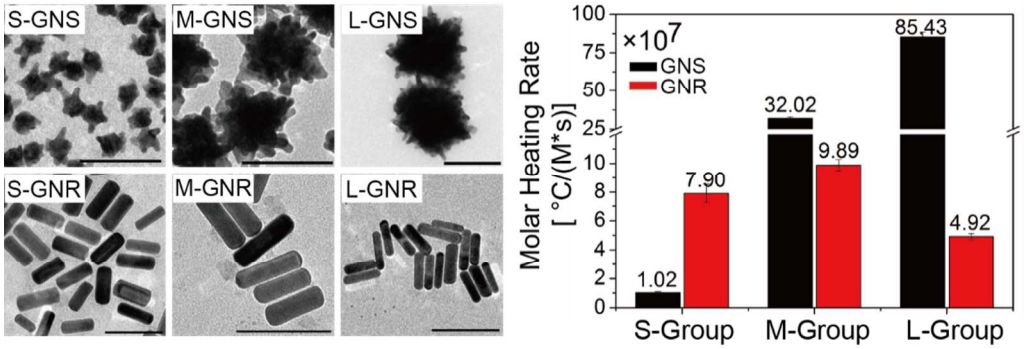

RSC Advances

RSCPublishing

ARTICLE

Understanding the Photothermal Effect of Gold Nanostars and Nanorods for Biomedical Applications

Cite this: DOI: 10.1039/x0xx00000x

Xiaocui Wang,[a b] Guohua Li,[a b] Yu Ding[a b] and Shuqing Sun[a *]

Received 00th January 2012,
Accepted 00th January 2012

DOI: 10.1039/x0xx00000x

www.rsc.org/

Plasmon-based photothermal effect of gold nanorod (GNR) has undergone the most systematic investigation for the cancer therapy in the biomedical realm. In recent years, gold nanostar (GNS) has come into sight with its attractive ability of transducing electromagnetic radiation into heat. The understanding the photothermal conversion efficiency is thus becoming more important for the selection of suitable materials for photothermal therapy. In this article, we investigated systematically the photothermal conversion efficiency and the molar heating rate of GNS and GNR in three groups (S-group, M-group and L-group, which represents groups of nanostructures with central extinction wavelength positioned at the shorter, medium and longer wavelength, respectively), to better understand the behaviour of GNS and GNR in the field of photothermal therapy. In M-group and L-group, the photothermal conversion efficiencies of GNSs and GNRs are similar, while GNSs have much higher molar heating rate than GNRs. Among all the samples, L-GNS has the highest molar heating rate, because of its large molar extinction coefficient. Meanwhile, dipole discrete approximation (DDA) is employed to simulate the optical properties of gold nanoparticles with different shape. And photothermal properties of GNSs and GNRs are compared both experimentally and theoretically. From both the experimental and theoretical results, M-GNS and L-GNS exhibit higher extinction efficiency than M-GNR and L-GNR, respectively.

1. Introduction

Hyperthermia has been used to destruct tumours for decades, and various heat sources, such as microwave,[1, 2] ultrasound[3] and laser light,[4, 5] have been employed to investigate thermal therapy. Laser-induced photothermal therapy for cancer treatment has been widely investigated, due to its ability of delivering specific amount energy directly to the cancerous tissue.[6-8] Near-infrared (NIR) light is an ideal electromagnetic source for the application of photothermal therapy, because it can transmit deeply in biological tissues.[9] There have been various kinds of nanomaterials employed in the field of photothermal therapy, such as hydrophilic flower-like CuS superstructures,[10] single-walled carbon nanotubes (SWNTs),[11, 12] graphene oxide,[13] gold nanospheres,[14] gold nanocages,[15, 16] gold nanoshells,[17, 18] gold nanopyramids,[19] gold nanorods (GNRs),[20, 21] and gold nanostars (GNSs).[22] These nanostructures have the ability to convert NIR light into heat on a picosecond timescale, which causes an increase of the temperature of the surrounding environment, and finally can lead to the damage of tumour cells.[23, 24]

GNR is a kind of ideal nanocrystal for the photothermal treatment of cancer and tumour. In the past years, GNRs have been extensively researched, and to some extent, GNRs have become a standard to evaluate the photothermal effects of other kinds of nanostructures. It has been found that the photothermal conversion efficiency of nanocrystals were strongly affected by several factors, such as plasmon resonance, shell coating, nanocrystal volume and assembly state.[25] To improve the photothermal efficiency and the heating speed of GNRs, a supercontinuum light can be used as a fast, energy efficient excitation source, together with femtosecond pulses.[26] In addition, biodegradable plasmonic vesicles, consisting of GNRs carrying mixed polymer brushes, also contributes to optimizing the photothermal conversion property of GNRs.[27] Because of the attractive photothermal conversion efficiency, GNRs have been used in vitro and in vivo, and have exerted outstanding curative effects. GNRs, which are covalently linked with

primary antibodies specific to the Gram-negative bacterium, can destroy Pseudomonas aeruginosa cells with high efficiency.[28] It is notable that the surface chemistry of GNRs has the dominant roles in the process of cellular uptake and negative charged GNRs can achieve a significant photothermal therapeutic benefit.[29, 30] Recently, a dual-function nano-system of photodynamic therapy (PDT) and photothermal therapy (PTT) has been remarkably synergistic for cancer cell treatment.[31, 32]

In recent years, GNS, as a new type of gold nanostructure, indicates its potential applications in biomedical areas, due to several outstanding properties. GNSs have multiple sharp tips, which act as 'hot spots' due to the 'lightning rod' effect.[33] Therefore, GNSs have been intensively used as substrates for application of surface enhanced Raman scattering spectroscopy (SERS).[34, 35] Besides the 'lightning rod' effect, GNSs also have tunable plasmon bands and strong absorption in NIR regions,[36] which enable GNSs to be an attractive nanoplatform in various biomedical fields, such as PTT,[37] PDT[38] and photoacoustic imaging.[39] Numerical calculations about the localized surface plasmon resonances of GNSs have already been performed through finite-difference time-domain (FDTD) method[40] and the 3D Green's Theorem method.[41] As GNSs have large absorption cross section in the range of near infrared wavelength, they show great potential in the field of photothermal therapy.[42] GNSs conjugated with specific nanobodies could cause cell damage under certain laser power density.[37] Moreover, GNSs linked with functionalized photosensitizer can be employed for the dual system of PDT and PTT to improve the anticancer effect and simplify the therapeutic process.[43] The photothermal conversion efficiency of GNSs can be enhanced greatly when they are coated with polypyrrole, and the polypyrrole shell contributes significantly to the structural stability of GNSs.[44]

In this article, the photothermal properties of three groups GNSs and GNRs with different plasmon resonance wavelength (683nm, 774nm, and 821nm) are measured and simulated. From the photothermal measurements, the photothermal conversion efficiencies of GNSs and GNRs are calculated and compared. At the same time, the molar heating rate, which has close relation with the photothermal conversion efficiency and the molar extinction coefficient, is calculated, and this parameter is more meaningful in practice for the photothermal applications. Besides, three optical parameters, including extinction efficiencies and absorption efficiencies are calculated, and these parameters are compared with the simulation results from discrete dipole approximation (DDA). It has been demonstrated that, GNSs, exhibiting large extinction coefficient, are also an excellent candidate for the photothermal treatment of cancer and tumours despite their large scattering cross section.

2. Experiment Section

2.1 Chemicals

Gold (III) chloride trihydrate ($HAuCl_4 \cdot 3H_2O$) was supplied by Sigma-Aldrich. Polyvinylpyrrolidone (PVP, MW=8000), cetyltrimethylammonium bromide (CTAB), sodium borohydride ($NaBH_4$), L-ascorbic acid (AA) were purchased from Alfa Aesar. N, N-dimethylformamide (DMF), hydrochloride (HCl, 37%), silver nitrate ($AgNO_3$), sodium citrate were purchased from local chemical companies. All the chemicals were used as received without any further purification. Ethanol and deionized water (18MΩ) were used for all experiments.

2.2 Preparation of GNSs and GNRs

We used seed-mediated growth method for the synthesis of both GNSs[36, 45] and GNRs.[46-48] Gold nanoparticles with smaller size were synthesized as seeds firstly, and then gold nanostructures of different shape were formed with the help of various surfactants.

2.2.1 Synthesis of GNSs. Water soluble gold nanoparticles of 16 nm were prepared according to the classical approach of standard citrate reduction. 50 mg of sodium citrate was dissolved in 50 mL of water, and 12.5 mL $HAuCl_4$ (1 mg/mL) was diluted to 100 mL with deionized water. Both solutions were heated in the water bath of 60 °C for about 30 minutes. Then the sodium citrate solution was added rapidly into the solution of $HAuCl_4$ with continuous stirring, and the temperature of water bath was increased to 85 °C and the mixed solution was heated for 2.5 h. The solution changed from light yellow to purple and finally it presented as clear wine red. After the gold colloid was cooled to room temperature, 1.2 mL of an aqueous solution of 0.1 g/mL PVP was added, and allowed to react over 24 h. The aqueous solution provided at least 60 molecules of PVP per square nanometres of gold nanoparticles, which could protect the gold nanoparticles from aggregating. Finally, the solution of gold nanoparticles capped by PVP was centrifuged at 10000 r/min for 30 min, the supernatant was discarded and the gold nanoparticles were redispersed in 2 mL of ethanol. For the growth of GNSs, 217 μL of 25.8 mM $HAuCl_4$ was mixed with 20 mL of 10 mM PVP solution in DMF. A certain volume of preformed seed dispersion was added rapidly into the PVP solution under continuous stirring and allowed to react in room temperature until completion of the reaction (no further changes in the colour of the mixture). In the experiment, we could get GNS with different sizes by varying the volume of seed dispersion. The GNSs colloid was centrifuged at 10000 rpm for 10 min, then the supernatant was removed and the branched nanoparticles were resuspended in deionized water for morphology and photothermal experiments.

2.2.2 Synthesis of GNRs. For the preparation of GNRs, 3-5 nm gold nanoparticles were synthesized at first. 38.1 μL of 25.8mM $HAuCl_4$ solution was mixed with 4 mL 100 mM CTAB solution. Then, 24 μL of 100 mM ice-cold $NaBH_4$ solution was added into the mixture all at once under vigorous stirring for 2 min, which resulted in the formation of a tea-brown seed solution. After the seed solution was stirred, it was kept at 25 °C at least 2 h for future use. For the growth of GNRs, 943 μL of 25.8mM $HAuCl_4$ solution was added into 50

mL 200 mM CTAB solution at 25 °C, and the mixture appeared bright yellow in colour. To this mixture, 375 μL of 5 M HCl solution, 120 μL of 40mM $AgNO_3$ solution and 400 μL of 100 mM fresh prepared AA solution were taken in sequence. Because of the mild reduction of AA, the growth solution changed from bright yellow to colourless. Finally, 70 μL of the seed solution was injected into the growth solution quickly and stirred for 30 seconds. The growth solution was allowed to stay undisturbed in a 30 °C thermostat overnight. GNRs with different aspect ratio could be obtained by changing the amount of $AgNO_3$. The obtained GNRs were purified by centrifugation at 7000 rpm for 10 min to remove the excess surfactant and were redispersed in deionized water for future use.

2.3 Instrumentation

We used an UV-Visible spectrophotometer (DU 800) to measure the extinction spectroscopy of gold nanostructures, and spectra were acquired every one minute depending on the scanning speed. Raw spectra were integrated from 400 to 1100 nm, with the wavelength step of 0.5 nm. Transmission electron microscopy (TEM) was performed to record the morphology of gold nanostructures using Tecnai G^2 30 instrument (120kV). To prepare samples for TEM, 8 μL of the gold colloid was deposited onto the copper grid and left to dry in air. Images were captured from different regions of each copper grid to determine the distribution of gold nanostructures.

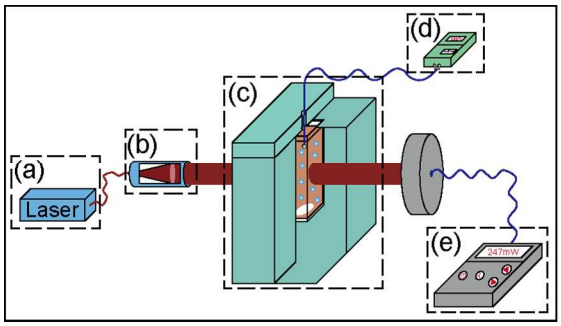

Scheme 1. Scheme of apparatus for measuring photothermal conversion efficiency of gold nanostructures. (a) Semiconductor diode laser with optical fibre outputing light with central wavelenth of 785 nm. (b) Lenses implanted into a hollow cylinder to change the light into parallel beam. (c) Sample cell, a quartz cuvette coated with foam plastic. (d) A thermometer with a K-type thermocouple probe to measure the temperature of the sample solution. (e) A power meter to record the laser power before and behind the sample solution.

2.4 Measurement of Photothermal Conversion Efficiency

The setup to measure the photothermal conversion efficiency is depicted in Scheme 1. A quartz cuvette (1 cm × 1 cm × 4 cm), which offered 10 mm light path, was filled up with the nanoparticle solution with a magnetic stir bar inside. In order to reduce the heat loss, the cuvette was covered with foam plastic remaining a pinhole for laser to pass through. A continuous semiconductor diode laser (785 nm, FC-785-500, SFOLT Co. Ltd, China) was coupled to an optical fibre with diameter of light spot of 7.5 mm. The nanoparticle solution was illuminated by the laser, and a power meter was used to measure the laser power. A K-type thermocouple probe (TP02A) was connected to a digital thermometer (TM902C) to record the temperature of the nanoparticle solution as a function of time. The probe head was immerged into the solution completely but away from the laser illumination area. During the measurement, a small teflon-coated magnetic bar was kept stirring to eliminate the temperature gradients of water in the sample cell.

2.5 DDA Simulations

DDA was used as a theoretical tool for the quantitative study of optical properties of gold nanostructure with various shape and size. The DDA calculations were performed using a software, OpenDDA, which ran on the Linux system.[49] The size and the shape of gold nanostructures were described to be identical to the TEM images. It was assumed that the gold nanostructures were placed in the 3D Cartesian coordinates. Typically, for GNRs, they were modelled like a cylinder with hemisphere caps, lying along the x-axis. As for GNSs, they were modelled as a sphere with six symmetrical branches, which were fixed along the x_+, x_-, y_+, y_-, z_+ and z_- direction, respectively, and the section plane of the branches is paraboloid. The gold nanostructures were divided into meshes of about 1 nm in size, and the incident light was set to be polarized along the x axis. The gold dielectric parameters were fitted with the interpolation method according to the experimental dielectric data, which was tabulated by Palik.[50] As the solvent was water, the refractive index of the surrounding medium was 1.333. The optical properties of GNRs and GNSs were quantified in the terms of extinction efficiency and absorption efficiency in the wavelength range of 400 to 1100 nm, the same range of UV-Visible extinction spectroscopy.

3. Results and Discussion

We prepared three GNS samples and three GNR samples, and these six gold nanostructures were classified into three groups according to their central extinction wavelength (S-Group, M-Group, and L-Group). Each group included a GNS and a GNR sample, both of which exhibited similar longitudinal plasmon wavelength (Figure 1a). In general, GNR samples have relatively narrower peak width than GNS samples, which is corresponding to the better monodispersity of GNRs. Figure 1b shows the TEM images of the GNS and GNR samples. To estimate the volume of GNRs, the morphology of more than 100 nanorods is surveyed. Because of the irregular growth of GNSs, it is difficult to measure the volume from the TEM images. So it is assumed that every GNS grows up from only one seed, and the volume of GNSs can be obtained if the total gold amount of the growth solution is known. Table 1 records the longitudinal plasmon peak position, concentration and average volume of each gold nanostructure sample. S-GNS shows fewer tips and is smaller in volume when compared to M-GNS and L-GNS. The tip number of each GNS is not constant, and the shape and position distribution of the tips are various. When the volume of GNS is small, the core made a significant contribution to the extinction spectroscopy, and the

extinction spectra shows two marked peaks. As the volume of GNS increases, the number of tips increases and the effect of the core on extinction spectra gradually decreases. Hence, the extinction peak of M-GNS and L-GNS becomes generally much wider, and the first extinction peak disappears. Instead, a general extinction across the whole spectra range appeared. As for GNRs, the average aspect ratio for S-GNR, M-GNR and L-GNR is 2.65, 3.78 and 4.18, respectively. With the increasing of the aspect ratio, the volume of these three GNR samples decreased. Through changing the concentration of the GNS and GNR solutions, the extinction intensities of the longitudinal plasmon peaks were adjusted to be between 0.8~1.0, which guaranteed that reasonable laser power could be recorded behind the quartz cuvette in the photothermal measurements. The concentration of these GNSs and GNRs samples varies from ~10 pM to ~500 pM, and it is displayed in Table 1.

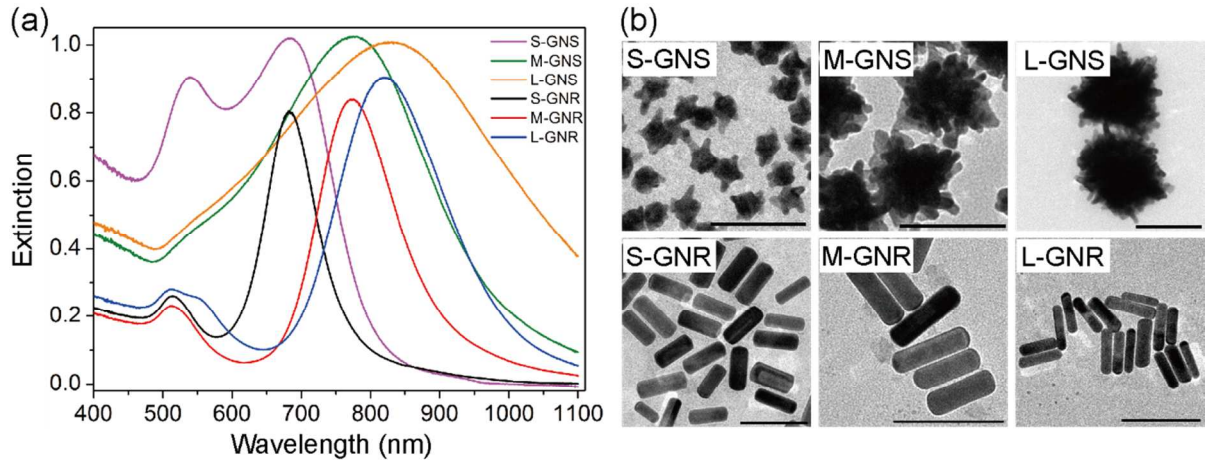

Figure 1. (a) UV-visible extinction spectra (cell path length: 1.0 cm) of the three groups GNS and GNR samples. In each group, GNS and GNR showed similar longitudinal plasmon peak. (b) TEM images of typical GNS and GNR samples used for photothermal conversion efficiency measurements. The scale bar of all the images is 100nm. The average lengths/diameters of GNRs are 63.8nm/24.5nm, 70.1nm/19.0nm, 56.9nm/13.9nm, respectively.

Table 1. Morphology characteristics of the gold nanostructures with representative longitudinal plasmon resonance peak, the laser power after passing through the sample cell and the extinction @785nm of the GNSs and GNRs. In this table, *c* represents the concentration of sample solution, and V represents the average volume of single gold nanoparticle.

GNS/GNR	Peak[nm]	*c*[pM]	V[nm^3]	Laser Power [mW]	Extinction
S-GNS	684.0	504.91	9483.5	126	0.2923
M-GNS	774.5	29.15	115268	22	1.0503
L-GNS	829.0	10.73	455290	23	1.0310
S-GNR	683.0	59.07	32159	151	0.2137
M-GNR	774.0	87.63	20557	48	0.7115
L-GNR	821.0	176.10	8993.5	54	0.6603

To calculate the photothermal conversion efficiency, we use a macroscopic model, which is similar to the ones expressed previously.[51-54] For any moment, the energy balance equations are described as below:

$$E_{ext} = E_{abs} + E_{sca} \quad (1)$$

$$E_{abs} = \sum_i m_i C_{p,i} \frac{dT}{dt} + E_{loss} \quad (2)$$

where E_{ext}, E_{abs} and E_{sca} are the extinction, absortion and scattering energy of nanostructures, respectively. Meanwhile, m_i and $C_{p,i}$ are the mass and the heat capacity of each composition of the sample cell, especially taking the constant pressure heat capacity of water as that of the nanostructure solution. The value of the solution parameters are m_s =3.7 g and $C_{p,s}$ = 4.187 J•g^{-1}•K^{-1}, and as for quartz cuvette, m_q = 6.4292 g and $C_{p,q}$ = 0.839 J•g^{-1}•K^{-1}. T is the temperature, t is the time, and E_{loss} is the energy dissipated by transferring to atmosphere. E_{ext}, E_{abs} and E_{loss} can be expressed as following:

$$E_{ext} = P(1-10^{-E}) \quad E_{abs} = \eta E_{ext} \quad E_{loss} = hS_A(T-T_0)$$

where P is the incident infrared laser power, E is the extinction of the nanostructure solution, η is the photothermal conversion efficiency, h is the heat transfer coefficient, S_A is the cross-sectional area perpendicular to the laser illumination, and T_0 is the ambient temperature.And then Eq. (2) can be recast into Eq. (3):

$$P(1-10^{-E})\eta = \sum_i m_i C_{p,i}\frac{dT}{dt} + hS_A(T-T_0) \quad (3)$$

Assuming a variable T^*, which is the temperature difference (T-T_0), Eq. (3) can be given as a simpler form in Eq. (4).

$$\frac{dT^*}{dt} = a - bT^* \quad (4)$$

In this equation, the parameter 'a' is the rate of absorption energy and the parameter 'b' is the rate constant related to heat loss, and they are described in Eq. (5).

$$a = \frac{P(1-10^{-E})\eta}{\sum_i m_i C_{p,i}} \qquad b = \frac{hS_A}{\sum_i m_i C_{p,i}} \quad (5)$$

Integrating Eq. (4) from 0 to t results in Eq. (6), which expresses the curve of temperature change in an exponent form.

$$T(t) = T_0 + \frac{a}{b}[1-\exp(-bt)] \quad (6)$$

By fitting the temperature curve, the value of parameters 'a' and 'b' can be get from the fitting parameters, which are used to calculate the experimental photothermal conversion efficiency η, defined in Eq. (7).

$$\eta = \frac{a\sum_i m_i C_{p,i}}{P(1-10^{-E})} \quad (7)$$

It is notable that the whole mass of the quartz cuvette does not contribute to the rise of temperature completely, thus the calibration of the effective mass of the quartz cuvette needs to be done. As for the calibration experiment, there is no laser and it is considered that the resistance R converts electrical energy into heat completely, i.e. E and the conversion efficiency η tend to be infinite and 1, respectively. Here, it is worthwhile to note that the battery should have small internal resistance, which ensures that the resistane has dominant differential voltage U. Then the parameter 'a' can be expressed simply as below:

$$a = \frac{P}{\sum_i m_i C_{p,i}} \quad (5')$$

In Eq (5'), the power P is considered as the heat power of the resistance, which is in proportion to U^2 and inversely proportional to R.

In the calibration experiment, a resistance, whose value is 30.31 Ω, has a differential voltage of 3.577 V. Therefore, the heat power of the resistance is 422 mW. The temperature was recorded every 30 s for 10 min as soon as the circuit was processed, and the data is shown into Figure 2a. Through fitting the temperature change curve using an exponential function, the parameter 'a' in Eq. (5') is found to be 0.02562. Therefore the effective mass of the quartz cuvette can be calculated, and it is $m_{q\text{-}eff}$ = 1.1741 g, less than 1/5 of the real mass of the quartz cuvette.

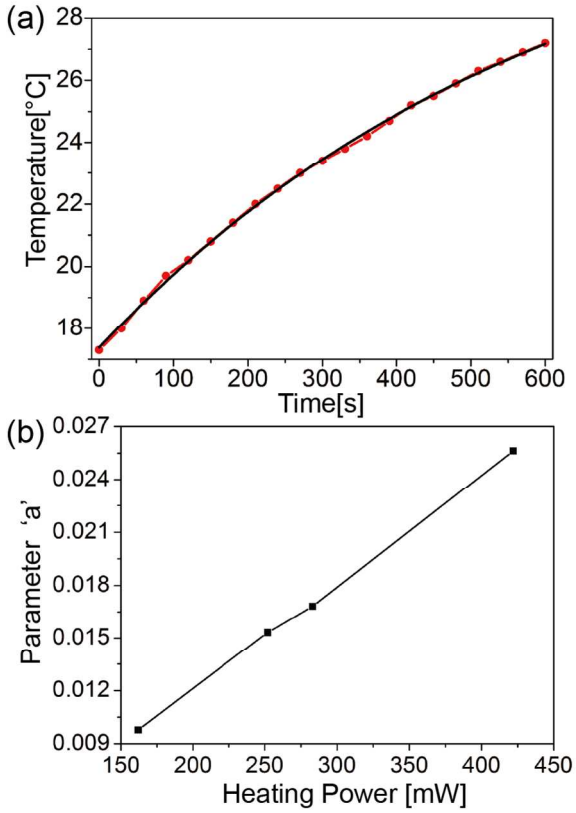

Figure 2. (a) The temperature change of water (red line with spot) as a function of time and exponential fitting (black line) used to calibrate the effective mass of quartz cuvette without laser illumination for the photothermal measurements of GNSs and GNRs. (b) The relationship between the parameter '*a*' and the heating power '*P*'.

To check the relationship between the parameter 'a' and the heating power P, several other resistances were hired to create different heating powers. The relationship is illustrated in Figure 2b, and it shows that the parameter 'a' is power dependent. The ratio of the heating power and the parameter 'a' is a constant, which means that the effective mass of the quartz cuvette is a constant.

With the calibration measurement, the representative curves of the temperature change of the GNSs and GNRs solutions in photothermal experiments can be obtained and are displayed in Figure 3a. In addition, the temperature change of water under laser illumination was measured. The temperature of the samples was recorded at different time, and all the starting point were set as t = 0. As the temperature of the environment are different, the starting temperature of each sample was different for different curves. The power of the laser before and after passing through the sample cell are both measured to calculate the extinction intensity E of the GNSs and GNRs according to the logarithm of the ratio of the laser power, i.e. $E = log_{10}(I_w/I_s)$, where I_w and I_s are the laser power behind water and the sample solution, respectively.

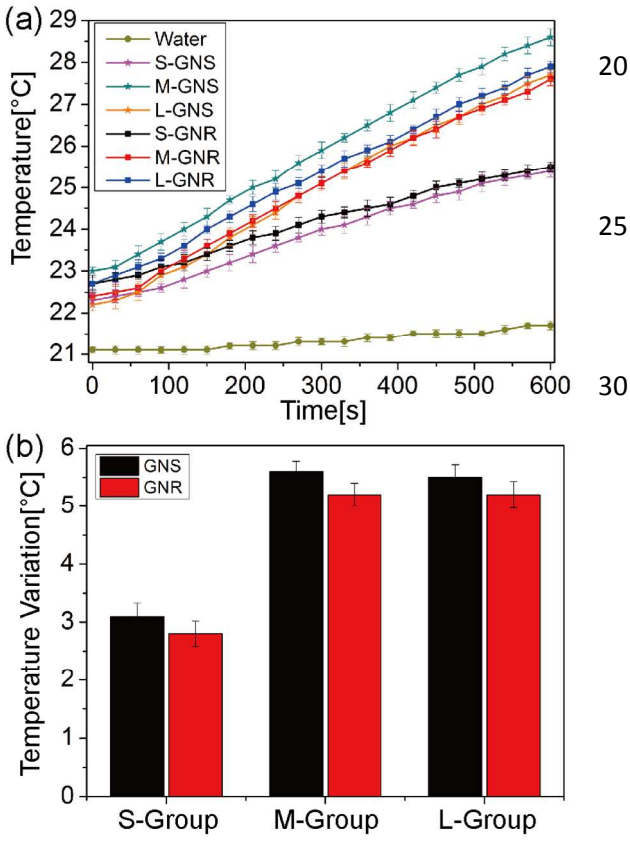

Figure 3. (a) Experimental data of GNSs and GNRs in aqueous solution under laser illumination to calculate the photothermal conversion efficiency. (b) The temperature variation comparison of GNSs (black bar) and GNRs (red bar) in three groups.

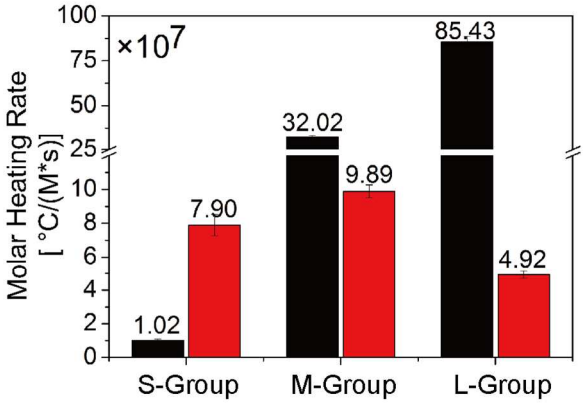

Figure 4. The molar heating rate of the GNSs (black bar) and GNRs (red bar) as the result of the temperature variation divided by the concentration.

The laser power before reaching the sample cell is 270 mW. The laser power I_w behind the sample cell containing water is 247 mW. Table 1 lists the laser power after the sample cell and the extinction of the six gold nanostructures obtained in the photothermal measurement. The temperature variation of the three groups samples is shown in Figure 3b. As the extinction peaks of S-GNS and S-GNR are away from 785 nm, their extinction values at 785 nm are much smaller than 1, which results in the less temperature variation when comparing with the M-group and L-group. According to the concentration in Table 1 and the temperature variation in Figure 3b, the molar heating rate can be given as the result of the temperature variation divided by the concentration (Figure 4). With the smallest concentration among all the six samples, L-GNS has the largest molar heating rate, more than 17 times larger than that of L-GNR. The difference between the molar heating rate indicates that the temperature in localized environment, containing specific concentration of L-GNS, will rise much faster than that with the same concentration of L-GNR. As for the S-GNS, its molar heating rate is smallest. In the M-group, the molar heating rate of GNS is about 3 times larger than that of GNR. In general, GNSs with large volume have a notable advantage in the molar heating rate over GNRs with the same longitudinal plasmon peaks.

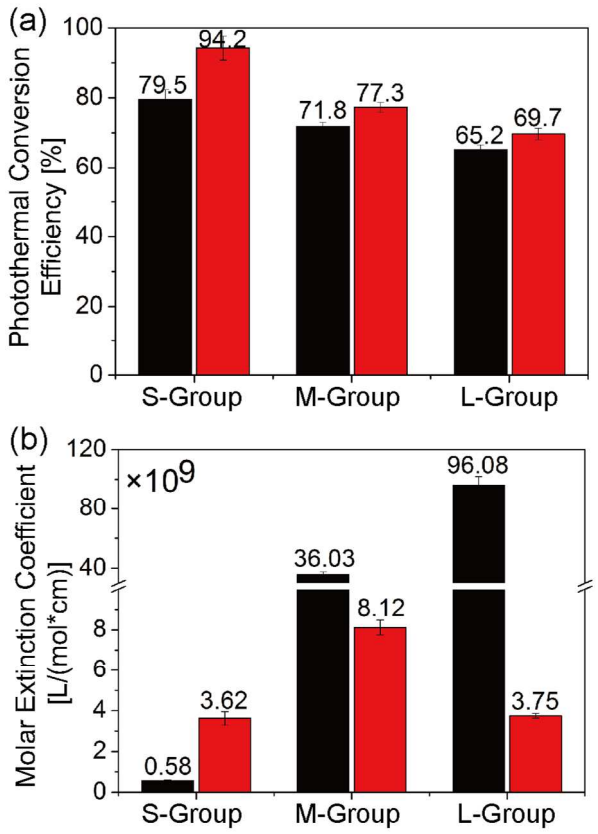

Figure 5. (a) Photothermal conversion efficiency of GNSs (black bar) and GNRs (red bar) , calculated by Eq. (7) according to the exponential fitting results. (b) The molar extinction coefficient of GNSs (black bar) and GNRs (red bar), calculated by Lambert-Beer law.

After fitting the temperature change curve of GNSs and GNRs, the parameter '*a*' in Eq. (5) of each sample can be obtained, and the photothermal conversion efficiency, shown in Figure 5a, can be calculated according to Eq. (7). Whether for GNSs or GNRs, the photothermal conversion efficiency decreases as the extinction peaks move from the visible region to the NIR region. The photothermal conversion efficiency of the S-group is higher than that of M-group and L-group. In the S-group, the S-GNR has a photothermal conversion efficiency

of 94.2%, which is the highest among all these six gold nanostructures. Although the photothermal conversion efficiency of S-GNS is lower than that of short GNR, it is yet higher than that of M-group and L-group. As for the M-group, the photothermal conversion efficiency of both GNS and GNR is over 70%. And the L-group has a photothermal conversion efficiency over 65%, which is about 1/3 lower than that of S-GNR. Considering the effect of particle volume on the photothermal conversion efficiency, there are similar results for these three groups. For each group, the photothermal conversion efficiency of GNS is lower than that of GNR, while the average volume of GNS is bigger than that of GNR, and this is coincident with previous research.[25, 51] The difference of the photothermal conversion efficiency between GNS and GNR varies for the three groups. Only in the S-group, photothermal conversion efficiency shows big gap between GNS and GNR. As the extinction peaks move to the NIR region, the efficiency gap between GNS and GNR becomes narrower to 5.5% and 4.5% for M-group and L-group, respectively.

According to the Lambert-Beer law, the extinction intensity of sample solution can be described like Eq. (8).

$$E = \varepsilon_{ext} cl \qquad (8)$$

In Eq. (8), ε_{ext} is the molar extinction coefficient of gold nanoparticles, c is the molar concentration of gold nanostructure solution, and l is the light path. The molar concentration and the extinction intensity of the gold nanoparticles are shown in Table 1. The optical path in our experiment is 10 mm. From the experimental data, the molar extinction coefficient of GNSs and GNRs can be calculated and the comparison is displayed in Figure 5b. In the S-group, whose plasmon peaks are away from 785 nm, the molar extinction coefficient of S-GNR is larger than that of S-GNS, while for both the M-group and L-group, GNSs have possess greater molar extinction coefficient than GNRs. As for the M-group, the molar extinction coefficient of M-GNS is about 4.5 times larger than that of M-GNR. And in the L-group, the gap between the molar extinction coefficient of L-GNS and L-GNR broadens, i.e. L-GNS holds more noticeable advantage over L-GNR. One main factor of the large molar extinction coefficient of M-GNS and L-GNS is that they occupy large volume (Table 1). What's more, because of the attractive molar extinction coefficient and the modest photothermal conversion efficiency, M-GNS and L-GNS have promising advantage in the process of transducing electromagnetic energy into, which indicates that they are prospective candidates in the field of photothermal therapy.

It is notable that the molar heating rate has close relation with the molar extinction coefficient and the photothermal conversion efficiency. Taking L-GNS for an example, it has the largest molar extinction coefficient, which means that every L-GNS has the strong ability to capture electromagnetic energy. At the same time, it has modest photothermal conversion efficiency, so it is able to convert electromagnetic energy into heat effectively. Therefore, the molar heating rate is a more practical parameter to evaluate the photothermal properties of different nanostructures in the biomedical realm.

It is generally known that the Avogadro constant N_A connects the macroscopic quantity and the microscopic quantity. The molar extinction coefficient ε_{ext} is the statistical optical parameter of gold nanoparticles, and it corresponds to the single nanoparticle extinction coefficient ε_{ext_s}, which is defined as $\varepsilon_{ext\_s} = \varepsilon_{ext} / N_A$. It is noticeable that the single nanoparticle extinction coefficient has the same dimension with the absorption cross section. Considering the different logarithm base of experimental molar extinction coefficient and theoretical extinction coefficient, the experimental extinction cross section is given as $C_{ext} = \tau \cdot \varepsilon_{ext\_s}$, in which τ is a constant of $ln10$. Furthermore, the extinction efficiency can be defined as the result of the extinction cross section divided by the effective cross-sectional area, i.e. $Q_{ext} = C_{ext}/\Pi_{eff}$. As mentioned previously,[25] the photothermal conversion efficiency depicts the effect of absorption in the extinction, thus the absorption efficiency can be given as $Q_{abs} = \eta \cdot Q_{ext}$ with the help of photothermal conversion efficiency. Hence, a set of experimental optical parameters of gold nanoparticles can be obtained. At the same time, DDA is a practical tool to simulate the optical properties of gold nanoparticles, and it outputs the extinction and the absorption efficiencies of samples. Therefore, DDA calculations are carried out to compare the theoretical optical parameters with the experimental ones.

The comparison of optical parameters of GNSs and GNRs is displayed in Figure 6, in which the first two frames are calculated from the photothermal measurement data, and the others are simulated using DDA. In Figure 6a and 6b, M-GNS and L-GNS hold slender advantage over M-GNR and L-GNR, which means that M-GNS and L-GNS have promising prospects in the field of photothermal therapy. In Figure 6a, the extinction efficiency of S-GNS is lower than that of S-GNR, while the extinction efficiency of M-GNS is larger than that of M-GNR, and the difference broadens in L-group. The same variation trend displays again about the absorption efficiency in Figure 6b. In all the three groups, M-GNS and L-GNS possess higher absorption efficiencies than M-GNR and L-GNR. When comparing the theoretical results and the experimental results, the difference may seem surprising at first glance. However, it should be noted that DDA simulates the optical properties of single nanoparticle, whereas the photothermal measurement is a statistical phenomenon. Furthermore, there are discrepancies between the real morphology of gold nanostructures and the geometric models applied in the DDA simulations. In Figure 6c and 6d, although the parameters of S-GNS do not hold obvious superiority when comparing with S-GNR, yet M-GNS and L-GNS has similar optical properties with M-GNR and L-GNR, which indicates that M-GNS and L-GNS can be used as photothermal agent like GNRs. As the central extinction peak of S-group is away from the laser wavelength, the extinction efficiencies of S-GNS and S-GNR are small at 785 nm, their application for photothermal therapy is limited, despite their high photothermal conversion efficiency. According to both experimental and theoretical results, M-GNS and L-GNS show

higher extinction efficiencies and absorption efficiencies than M-GNR and L-GNR, indicating M-GNS and L-GNS are promising materials for the photothermal treatment of cancer and tumours.

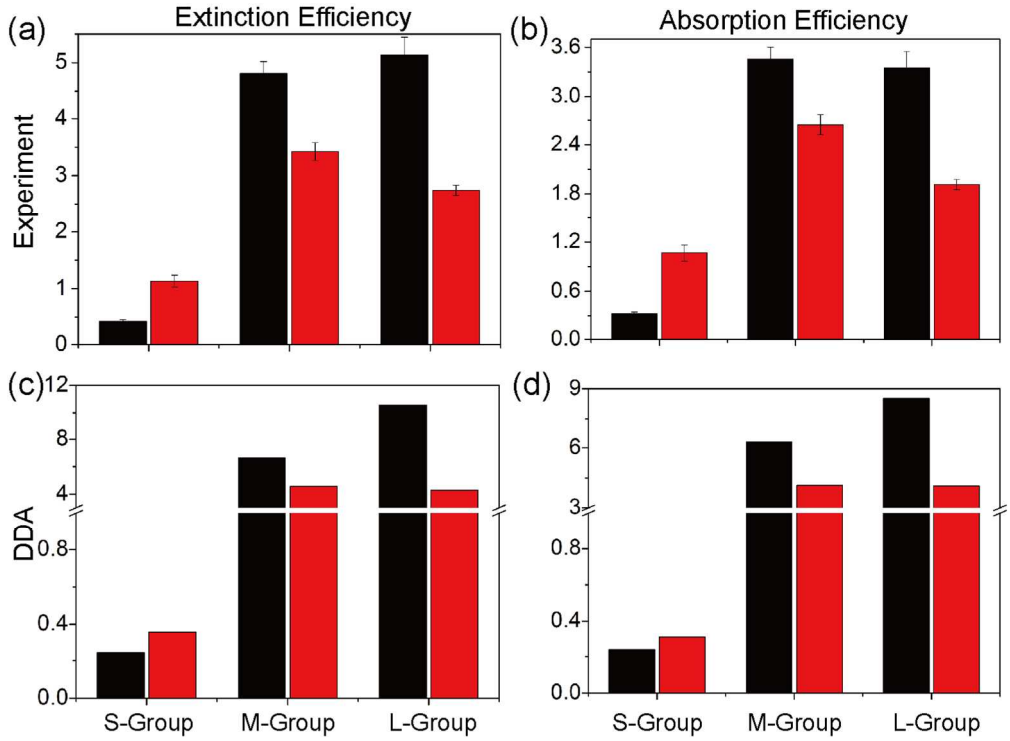

Figure 6. The typical optical parameters of GNSs (black bar) and GNRs (red bar), including extinction efficiency, absorption efficiency and scattering efficiency, calculated both from experiment (a, b) and DDA (c, d), respectively.

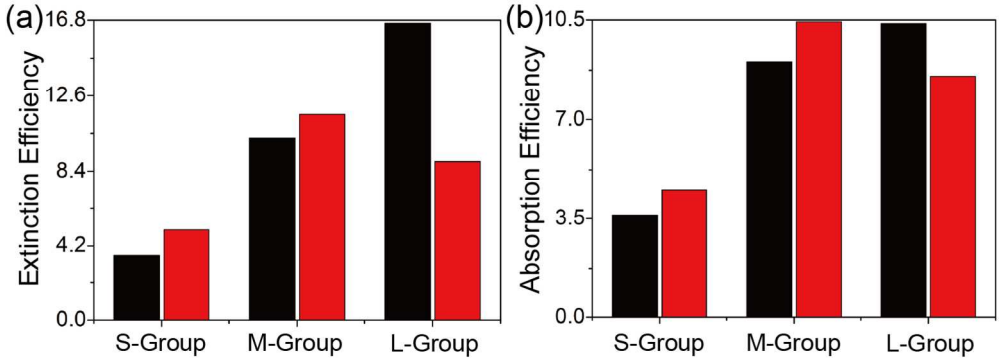

Figure 7. The simulated extinction efficiencies (a) and absorption efficiencies (b) of GNSs (black bar) and GNRs (red bar) at their central plasmon resonant peaks, respectively.

From the comparative study of GNSs and GNRs, the S group usually has little advantages, except for the photothermal conversion efficiency, and this is because the central plasmon resonant peak of S group is far away from the NIR laser wavelength. To check the photothermal properties at the plasmon peak, DDA was used to calculate the extinction efficiency and the absorption efficiency of all the three groups of gold nanostructures at their own central plasmon resonant peak, and the simulation result is illustrated in Figure 7. In general, the simulation results at the plasmon peak are all higher than that at the NIR laser wavelength. It is obvious that the extinction efficiency and the absorption efficiency of S group are much larger than that in Figure 6c and 6d. While M group and L group does not show large difference between the simulation results at plasmon peak and the simulation values at the NIR laser wavelength. The simulation results indicate that the gold nanostructures show best photothermal performance at their own plasmon resonant peak. However, as mentioned above, the biological tissues are highly transparent to NIR light, while the central plasmon resonant peak of S group is in visible region. Therefore, the optical parameters of S group at the central peak are of less practical significance for photothermal therapy.

4. Conclusions

In summary, the temperature variation of three groups GNSs and GNRs has been recorded with calibration of the effective mass of the container and the photothermal conversion efficiency of each sample has been calculated, according to an exponential model of temperature change. Due to the different extinction intensity at the illumination laser wavelength, the aqueous solution of M-group and L-group gold nanostructures can reach higher temperature than S-group. The photothermal conversion efficiency of gold nanostructures depends strongly on the morphology, the plasmon resonance wavelength and the nanostructure volume. Although gold nanoparticles in S-group provide higher photothermal conversion efficiency, gold nanoparticles in M-group and L-group possess faster molar heating rate and larger molar extinction coefficient, which means that they can satisfy specific heating requirements with less time and fewer nanoparticles. DDA is employed to simulate the optical properties of gold nanoparticles. It should be noted that, biological tissues are highly scattering medium, and our research are conducted in a non-participating medium. Nevertheless, both experimental and theoretical results show that GNSs have similar photothermal properties with GNRs, especially for M-GNS and L-GNS, which paves way to the potential application of GNSs in the field of cancer photothermal therapy.

Acknowledgements

The work was supported by the National Nature Science Foundation of China (grants no 212731126) and Fundamental Research Program of Shenzhen (JC201105201112A, JCYJ20120619151629728). Part of this work was supported by Open Research Fund Program of the State Key Laboratory of Low-Dimensional Quantum Physics (KF201311).

Notes and references

[a] Shenzhen Key Laboratory for Minimal Invasive Medical Technologies, Graduate School at Shenzhen, Tsinghua University, Shenzhen, 518055, China.

[b] Department of Physics, Tsinghua University, Beijing 100084, China.

* E-mail: sun.shuqing@sz.tsinghua.edu.cn.

1. T. Seki, M. Wakabayashi, T. Nakagawa, M. Imamura, T. Tamaki, N. Nishimura, N. Yamashiki, A. Okamura and K. Inoue, *Cancer*, 1999, **85**, 1694.
2. G. S. Gazelle, S. N. Goldberg, L. Solbiati and T. Livraghi, *Radiology*, 2000, **217**, 633.
3. F. A. Jolesz and K. Hynynen, *Cancer J. (Sudbury, Mass.)*, 2001, **8**, S100.
4. S. M. Waldow, P. R. Morrison and L. I. Grossweiner, *Lasers Surg. Med.*, 1988, **8**, 510.
5. W. R. Chen, R. L. Adams, R. Carubelli and R. E. Nordquist, *Cancer Lett.*, 1997, **115**, 25.
6. R. Puls, C. Stroszczynski, G. Gaffke, N. Hosten, R. Felix and U. Speck, *J. Magn. Reson. Imaging*, 2003, **17**, 663.
7. A. Vogel and V. Venugopalan, *Chem. Rev.*, 2003, **103**, 577.
8. D. P. O'Neal, L. R. Hirsch, N. J. Halas, J. D. Payne and J. L. West, *Cancer Lett.*, 2004, **209**, 171.
9. N. W. S. Kam, M. O'Connell, J. A. Wisdom and H. Dai, *Proc. Natl. Acad. Sci. U. S. A.*, 2005, **102**, 11600.
10. Q. Tian, M. Tang, Y. Sun, R. Zou, Z. Chen, M. Zhu, S. Yang, J. Wang, J. Wang and J. Hu, *Adv. Mater.*, 2011, **23**, 3542.
11. Y. Shen, A. G. Skirtach, T. Seki, S. Yagai, H. Li, H. Möhwald and T. Nakanishi, *J. Am. Chem. Soc.*, 2010, **132**, 8566.
12. L. F. Neves, J. J. Krais, B. D. Van Rite, R. Ramesh, D. E. Resasco and R. G. Harrison, *Nanotechnology*, 2013, **24**, 375104.
13. Z. Sheng, L. Song, J. Zheng, D. Hu, M. He, M. Zheng, G. Gao, P. Gong, P. Zhang and Y. Ma, *Biomaterials*, 2013, **34**, 5236.
14. X.-D. Zhang, D. Wu, X. Shen, J. Chen, Y.-M. Sun, P.-X. Liu and X.-J. Liang, *Biomaterials*, 2012, **33**, 6408.
15. J. Chen, D. Wang, J. Xi, L. Au, A. Siekkinen, A. Warsen, Z.-Y. Li, H. Zhang, Y. Xia and X. Li, *Nano Lett.*, 2007, **7**, 1318.
16. S. E. Skrabalak, J. Chen, Y. Sun, X. Lu, L. Au, C. M. Cobley and Y. Xia, *Acc. Chem. Res.*, 2008, **41**, 1587.
17. M. P. Melancon, W. Lu, Z. Yang, R. Zhang, Z. Cheng, A. M. Elliot, J. Stafford, T. Olson, J. Z. Zhang and C. Li, *Mol. Cancer Ther.*, 2008, **7**, 1730.
18. C. Loo, A. Lowery, N. Halas, J. West and R. Drezek, *Nano Lett.*, 2005, **5**, 709.
19. W. Hasan, C. L. Stender, M. H. Lee, C. L. Nehl and J. Lee, *Nano Lett.*, 2009, **9**, 1555.
20. X. Huang, I. H. El-Sayed, W. Qian and M. A. El-Sayed, *J. Am. Chem. Soc.*, 2006, **128**, 2115.
21. A. M. Alkilany, L. B. Thompson, S. P. Boulos, P. N. Sisco and C. J. Murphy, *Adv. Drug Delivery Rev.*, 2012, **64**, 190.
22. H. Yuan, C. G. Khoury, C. M. Wilson, G. A. Grant, A. J. Bennett and T. Vo-Dinh, *Nanomed. Nanotechnol. Biol. Med.*, 2012, **8**, 1355.
23. F. Zhou, S. Wu, B. Wu, W. R. Chen and D. Xing, *Small*, 2011, **7**, 2727.
24. E. Miyako, K. Kono, E. Yuba, C. Hosokawa, H. Nagai and Y. Hagihara, *Nat. Commun.*, 2012, **3**, 1226.
25. H. Chen, L. Shao, T. Ming, Z. Sun, C. Zhao, B. Yang and J. Wang, *Small*, 2010, **6**, 2272.
26. W. Tao, H. Bao and M. Gu, *Appl. Phys. B*, 2013, **112**, 153.
27. J. Song, L. Pu, J. Zhou, B. Duan and H. Duan, *ACS Nano*, 2013, **7**, 9947.
28. R. S. Norman, J. W. Stone, A. Gole, C. J. Murphy and T. L. Sabo-Attwood, *Nano Lett.*, 2008, **8**, 302.
29. Y. Qiu, Y. Liu, L. Wang, L. Xu, R. Bai, Y. Ji, X. Wu, Y. Zhao, Y. Li and C. Chen, *Biomaterials*, 2010, **31**, 7606.
30. S. Jin, X. Ma, H. Ma, K. Zheng, J. Liu, S. Hou, J. Meng, P. C. Wang, X. Wu and X.-J. Liang, *Nanoscale*, 2013, **5**, 143.
31. J.-Y. Kim, W. I. Choi, M. Kim and G. Tae, *J. Controlled Release*, 2013, **171**, 113.
32. J. Lin, S. Wang, P. Huang, Z. Wang, S. Chen, G. Niu, W. Li, J. He, D. Cui and G. Lu, *ACS Nano*, 2013, **7**, 5320.
33. S. Abalde-Cela, P. Aldeanueva-Potel, C. Mateo-Mateo, L. Rodríguez-Lorenzo, R. A. Alvarez-Puebla and L. M. Liz-Marzán, *J. R. Soc. Interface*, 2010, **7**, S435.
34. C. G. Khoury and T. Vo-Dinh, *J. Phys. Chem. C*, 2008, **112**, 18849.

35. H. Yuan, A. M. Fales, C. G. Khoury, J. Liu and T. Vo‐Dinh, *J. Raman Spectrosc.*, 2013, **44**, 234.
36. S. Barbosa, A. Agrawal, L. Rodríguez-Lorenzo, I. Pastoriza-Santos, R. A. Alvarez-Puebla, A. Kornowski, H. Weller and L. M. Liz-Marzán, *Langmuir*, 2010, **26**, 14943.
37. B. Van de Broek, N. Devoogdt, A. D'Hollander, H.-L. Gijs, K. Jans, L. Lagae, S. Muyldermans, G. Maes and G. Borghs, *ACS Nano*, 2011, **5**, 4319.
38. A. M. Fales, H. Yuan and T. Vo-Dinh, *Langmuir*, 2011, **27**, 12186.
39. C. Kim, H.-M. Song, X. Cai, J. Yao, A. Wei and L. V. Wang, *J. Mater. Chem.*, 2011, **21**, 2841.
40. F. Hao, C. L. Nehl, J. H. Hafner and P. Nordlander, *Nano Lett.*, 2007, **7**, 729.
41. R. Rodríguez-Oliveros and J. A. Sánchez-Gil, *Opt. Express*, 2012, **20**, 621.
42. H. Yuan, A. M. Fales and T. Vo-Dinh, *J. Am. Chem. Soc.*, 2012, **134**, 11358.
43. S. Wang, P. Huang, L. Nie, R. Xing, D. Liu, Z. Wang, J. Lin, S. Chen, G. Niu and G. Lu, *Adv. Mater.*, 2013, **25**, 3055.
44. J. Li, J. Han, T. Xu, C. Guo, X. Bu, H. Zhang, L. Wang, H. Sun and B. Yang, *Langmuir*, 2013, **29**, 7102.
45. D. C. Hone, A. H. Haines and D. A. Russell, *Langmuir*, 2003, **19**, 7141.
46. B. Nikoobakht and M. A. El-Sayed, *Chem. Mater.*, 2003, **15**, 1957.
47. T. K. Sau and C. J. Murphy, *Langmuir*, 2004, **20**, 6414.
48. J. Cheng, L. Ge, B. Xiong and Y. He, *J. Chin. Chem. Soc.*, 2011, **58**, 822.
49. J. Mc Donald, A. Golden and S. G. Jennings, *Int. J. High Perform. Comput. Appl.*, 2009, **23**, 42.
50. E. D. Palik, *Handbook of Optical Constants of Solids*, Academic Press, New York, 1985.
51. J. R. Cole, N. A. Mirin, M. W. Knight, G. P. Goodrich and N. J. Halas, *J. Phys. Chem. C*, 2009, **113**, 12090.
52. H. H. Richardson, M. T. Carlson, P. J. Tandler, P. Hernandez and A. O. Govorov, *Nano Lett.*, 2009, **9**, 1139.
53. D. K. Roper, W. Ahn and M. Hoepfner, *J. Phys. Chem. C*, 2007, **111**, 3636.
54. D. K. Kim, M. S. Amin, S. Elborai, S.-H. Lee, Y. Koseoglu, M. Zahn and M. Muhammed, *J. Appl. Phys.*, 2005, **97**, 10J510.

